Helicene-bis-porphyrin conjugates: exciton coupling chirality and chiral-induced spin selectivity

Paola Matozzo,[1] Kakali Santra,[2] Anil Kumar,[2] Saurav Parmar,[3] Pierpaolo Morgante,[3] Kais Dhbaibi,[1] Rajatha Rajendran,[1] Nicolas Vanthuyne,[4] Ron Naaman,[2,*] Jochen Autschbach,[3,*] Jeanne Crassous,[1,*]

[1] Dr. P. Matozzo, Dr. K. Dhbaibi, R. Rajendran, Dr. J. Crassous
Institut des Sciences Chimiques de Rennes
University of Rennes, CNRS, ISCR
UMR 6226, F-35000 Rennes, France
E-mail: jeanne.crassous@univ-rennes.fr

[2] Dr. A. Kumar, Dr. K. Santra, Prof. Dr. R. Naaman
Department of Chemical and Biological Physics
Weizmann Institute of Science
Rehovot 76100, Israel
E-mail: ron.naaman@weizmann.ac.il

[3] Dr. Pierpaolo Morgante, Dr. Saurav Parmar, Prof. Jochen Autschbach
Department of Chemistry, University at Buffalo,
State University of New York, Buffalo, New York 14260, USA.
E-mail: jochena@buffalo.edu

[4] Dr. N. Vanthuyne
Aix Marseille Univ, CNRS, Centrale Med, FSCM, Marseille, France

Abstract

Following our previous work on helicene-porphyrin conjugates in which carbo[6]helicene were connected to zinc-porphyrin via phenyl-bis-ethynyl bridges (**Por(Zn)-H[6]^{1}**, series 1), and displaying clear exciton coupling (EC) chirality, we prepared novel carbo[6]helicenes derivatives substituted at their 2,15 positions by zinc-porphyrin units, either through a triple bond (**Por(Zn)-H[6]^{2}**, series 2), or through an alkynyl-phenyl bridge (**Por(Zn)-H[6]^{3}**, series 3). Series 2 was also synthesized with free porphyrins or different metals [Ni(II), and Pd(II)]. Their photophysical and chiroptical properties (electronic circular dichroism and circularly polarized luminescence) were characterized, and it was examined how i) the distance between the porphyrin units and ii) the metal type impacted these properties. Experimental and theoretical analyses highlight strong responses originating from EC chirality in combination with the typical helicene-centered optical activity. The **Por(Zn)-H[6]^{2}** system displaying strong absorption dissymmetry factors was then selected to experimentally examine the chiral induced spin selectivity (CISS) effect by magnetic conductive atomic force microscopy (mc-AFM); a spin polarization of 50% was measured.

Introduction

Helicenes are helical π-conjugated molecules formed of *ortho*-fused aromatic rings. They exhibit strong chiroptical properties (very high specific optical rotations – OR, intense electronic circular dichroism – ECD, and strong molecular circularly polarized luminescence – CPL) which are appealing in a variety of research fields, such as optoelectronics, spintronics or biological imaging.[1] Recently, it has been shown that grafting two achiral chromophores at the 2,15 extremities of a carbo[6]helicene scaffold enables to efficiently tune and enhance the

chiroptical activity. Indeed, because the π–conjugation through the whole helical backbone is limited, covalently grafted achiral chromophores can interact through space, and give access to Exciton Coupling (EC) chirality.[2] It is well-known that when two or more identical chromophores are connected to vicinal functions such as diols, diamines or other, within a chiral molecule, they may interact with each other through space and give rise to EC chirality. EC may lead to intense ECD, consisting of bisignate Cotton effects, from the sign of which the absolute configuration of the molecule can be deduced. Berova, Harada and Nakanishi have pioneered this domain, developed the nonempirical approach called 'CD Exciton Chirality Method', and exhaustively used it to determine absolute configurations of many classes of chiral compounds and natural products.[3] Typically, the achiral chromophores used in such research exhibit a strong transition electric dipole moment in preferred directions. Porphyrins are archetypes of such chromophores[4] since they display i) highly intense absorption bands, especially the Soret band (epsilon > 10^5 M^{-1} cm^{-1}), ii) planar geometry and iii) an ability to coordinate metal ions.[5] In 2021, we described the first example of helicene-porphyrin conjugates to explore and rationalize the role of the helical π-conjugation in the EC phenomenon.[6] We showed that grafting two ethynyl-porphyrin units on the 2,15 positions of a carbo[6]helicene results in a clear, strong EC signature due to the Soret band, with the appearance of an isolated bisignate ECD couplet at 440 nm. In this prior work, the synergetic effect of helicenes and porphyrins in obtaining enhanced chiroptical responses in an absorption region was highlighted.

Recently, chiral induced spin selectivity (CISS) has emerged as a highly active area of research and a fascinating topic that connects chirality, charge transport and magnetism.[7] In this domain, the strong polarizabilities and the long spin relaxation times of porphyrins have demonstrated their benefit in effectively maintaining the spin polarization through a chiral system formed of a L-proline octamer conjugated with a (porphinato)zinc organized into a Self-Assembled Monolayer (SAM) onto a gold-nickel substrate via a thiolate unit.[8] Magnetic conducting atomic force microscopy (mc-AFM), spin-dependent electrochemistry, and spin Hall devices were capable of measuring the spin polarizability that accompanies charge polarization. Likewise, owing to their strong chiroptical responses and semi-conducting properties, helicenes have revealed efficient spin filtering properties.[9]

Only few helicene-porphyrinoids (porphyrin, phtalocyanines, or porphyrazins) systems have been reported in the literature thus far.[10] However, even though the absorption domain could be efficiently tuned down to the near-infrared (NIR) region and a strong ECD response of the Soret band could be observed in most cases, none of these examples displayed a bisignate EC signature except the helicene-bis-porphyrine conjugates (**Por(H_2)-H[6]^1** and **Por(Zn)-H[6]^1** in Figure 1) described by our team in 2021.[6] Herein, we explore this novel class of helicene-porphyrin conjugates by preparing new series of carbo[6]helicenes substituted at their 2,15 positions by porphyrin units either through a triple bond (**Por(Zn)-H[6]^2**), or through an alkynyl-phenyl bridge (**Por(Zn)-H[6]^3**). In this way, we are able to control the distance between the two porphyrin units and investigate the impact on the photophysical and chiroptical properties of the Zn(II) derivatives and, in particular, the EC response. In series 2, we prepared the free porphyrins, together with diverse metal complexes [Zn(II), Ni(II), and Pd(II)]. These metallic ions were chosen for their different coordination geometries, electronic structures, and optical properties. The resulting experimental photophysical and chiroptical properties were characterized in detail. Furthermore, with the help of theoretical calculations it was examined

how the metal ion impacts in particular the EC signature. The **Por(Zn)-H[6]^2** system was further selected to be experimentally studied by mc-AFM in order to investigate its spin filtering ability.

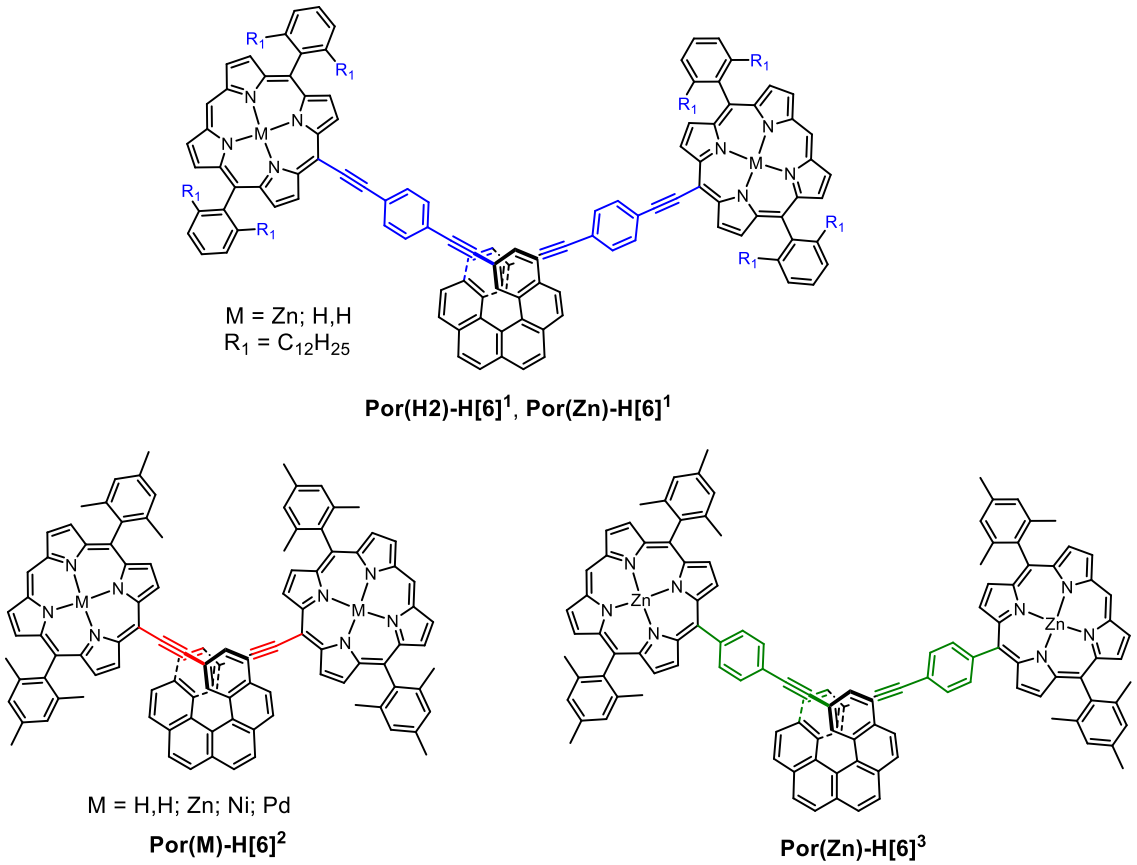

Figure 1. Different types of carbo[6]helicene-bis-porphyrin conjugates **Por(M)-H[6]$^{1\text{-}3}$** examined by varying the spacer between the helicene and porphyrin units (alkynyl-phenyl-alkynyl in series 1, alkynyl in series 2, and alkynyl-phenyl in series 3.

Results and discussion

Synthesis of helicene-bis-ethynyl-porphyrin systems (Por(M)-H[6]^2)

The first derivative was designed starting from the already known enantiopure *P* and *M*-2,15-bis-ethynyl-carbo[6]helicene (**H[6]**) building blocks.[11] In order to avoid the presence of Glaser by-products, which appeared particularly efficient in the case of a copper-free Sonogashira reaction[12] was set-up between the ethynyl-helicene and the brominated free porphyrin (Scheme 1), giving the desired compounds **Por(H2)-H[6]^2** with 45% yield (see Electronic Supplementary Information, ESI). The Zn(II), N(II), and Pd(II) complexes, *i.e.* **Por(Zn)-H[6]^2**, **Por(Ni)-H[6]^2**, and **Por(Pd)-H[6]^2**, were then obtained by metalation of the free-base **Por(H2)-H[6]^2** according to Scheme 1 and following classical procedures (see the ESI). All these derivatives were fully characterized by ^{1}H and ^{13}C NMR spectroscopy and mass spectrometry (see Supporting Snformation, SI). As an example, the ^{1}H-NMR spectrum of the free base derivative **Por(H2)-H[6]^2**, with the respective assignments for all the protons, is reported on Figure S1.8 In contrast to the previously described **Por(H2)-H[6]^1**,[6] the helicene unit shows a well-defined set of peaks: the "external" protons resonate as 5 different doublets from 8.31 to

7.98 ppm, while the protons placed at the *ortho* position with respect to the triple bond, *i.e.* at the 1,16 inner positions of the helix, resonate as a singlet at 8.57 ppm. Except from the protons on the free porphyrin-helicene derivative, in which the NHs resonate at -2.44 ppm and are not present for the coordinated-porphyrin derivatives, the signal pattern of the chromophore in the **Por(M)-H[6]^2** series remained unaffected by changing the metal. The mass of all these new compounds was ascertained by MALDI experiments (see SI).

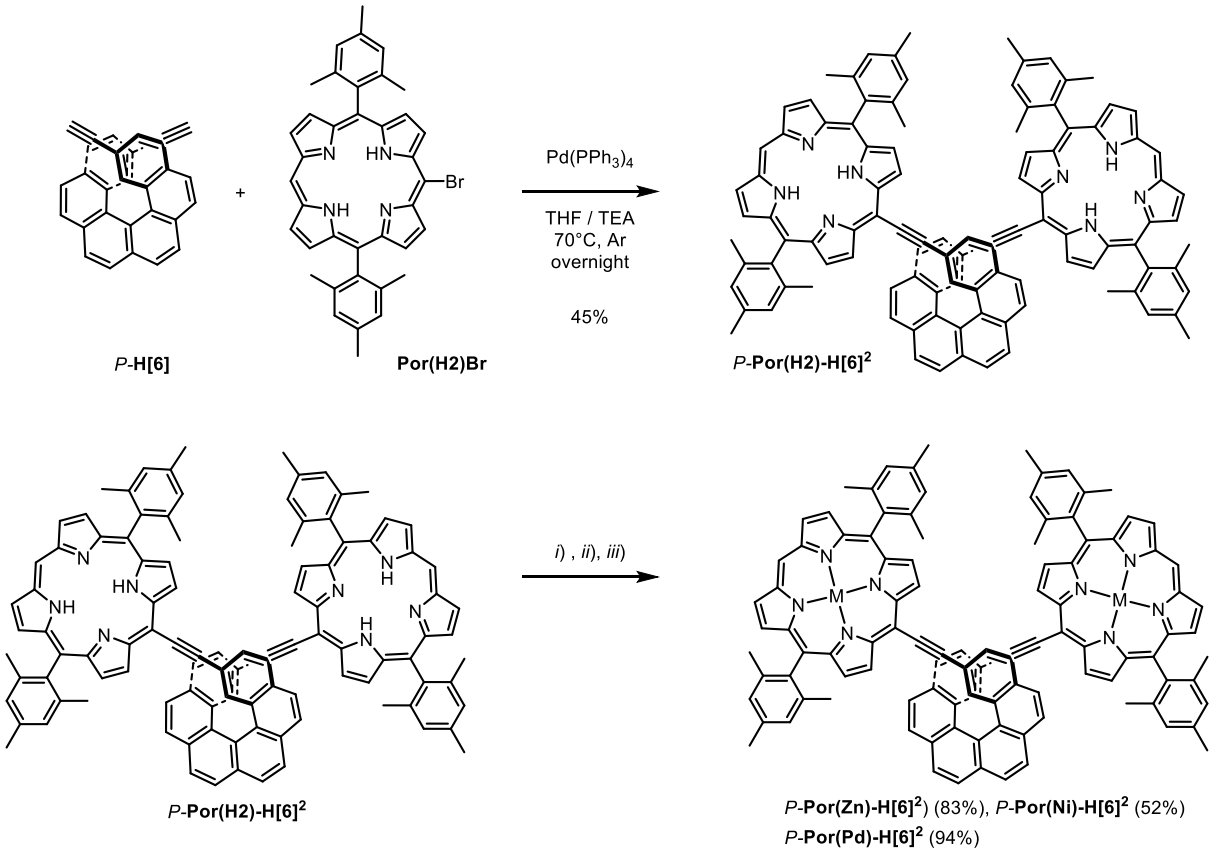

Scheme 1. Synthetic route to enantiopure helicene-bis-ethynyl-porphyrine derivatives *P*-**Por(M)-H[6]^2**. *i*) $Zn(OAc)_2$•$2H_2O$, $CHCl_3$/MeOH, 4 hrs, rt; *ii*) $Ni(OAc)_2$•$4H_2O$, DMF, 12 hrs, 150°C; *iii*) $PdCl_2$, PhCN/DMF, 4h, 150°C, Ar.

Structural characterization by molecular modelling of (Por(M)-H[6]^2) series

The molecular structures were optimized with density functional theory (DFT) and give a clearer idea about the helicenic environment and of the porphyrin unit geometries (Figure 2 and SI). In **Por(H2)-H[6]^2**, the optimized porphyrins were found fully planar and the mesityl substituents fully perpendicular to them. In this structure, the porphyrin displayed coplanarity with the terminal ring of the helicene unit (dihedral angle between both units of around 2.1°) thus ensuring efficient conjugation through the ethynyl bridge. Moreover, the helicity (i.e. dihedral angle between the two terminal rings) displays a 52° value which is typical for carbo[6]helicenes.[1] Interestingly, the theoretical centroid-centroid distance between the two porphyrin units was found to be of 15.5 Å. Overall, the two porphyrin units display a mutual orientation (dihedral angle between both porphyrin cycles) of 56°. Very similar features were found for model structures in which mesityl groups were changed to chlorine atoms; a model of such a full (containing mesityl groups) and the substituted molecule is illustrated in Figure

2. Further discussion related to the full vs. truncated models can be found in the SI. The Cl-truncated models were used for a subset of the calculations, to keep the computational effort manageable.

The zinc complex **Por(Zn)-H[6]^2** substantially displayed the same structural features as the protonated one, namely full planarity of the zinc-porphyrin units, efficient conjugation between porphyrin and terminal cycles via the ethynyl bond but with a slightly higher dihedral angle between both units of around 8°, a helicity of 50° of the helical core, and an optimized distance between the two Zn atoms of 15Å. Note that in this case the two porphyrin units display an overall mutual orientation of 34.3°. Regarding the **Por(Ni)-H[6]^2** derivative, it was necessary to remove the mesityl groups to fully converge to an optimized structure, with the typical porphyrin units displaying a ruffle-type topology.[13] A helicity of 52° was measured for the helicenic core, with again efficient conjugation between each porphyrin and terminal aromatic cycle of the helix linked through the ethynyl bridge. Interestingly, the Ni-Ni distance is found around 15.3 Å, that is very similar to the other derivatives **Por(H2)-H[6]^2** and **Por(Zn)-H[6]^2**. Structurally, the Pd(II) and Cu(II) complexes **Por(Pd)-H[6]^2** and **Por(Cu)-H[6]^2** were found to display the same features as the Zn(II) derivatives with similar metrics, for instance a helicity of 52°, a metal-metal distance of 15.5 Å and full planarity of the porphyrin units.

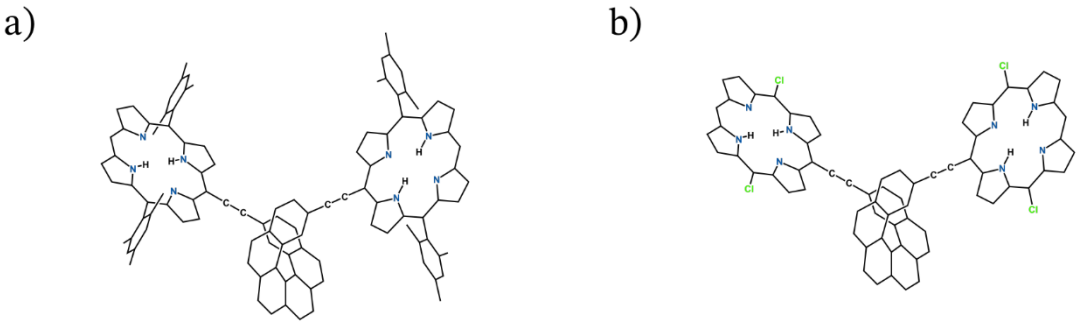

Figure 2. a) Representation of **Por(H2)-H[6]^2** (containing mesityl groups) free-base, b) Representation of a **Por(H2)-H[6]^2** chlorinated free-base. Hydrogens (except inside the porphyrin rings) not shown for clarity.

Absorption properties (UV-vis and ECD spectroscopies) of Por(M)-H[6]^2 series

Due to their 18 π-electrons, porphyrins are macrocycles with extended aromaticity, and their absorption occurs in the visible range. Thanks to their extremely high molar extinction coefficients, porphyrins and their derivatives are among the most intense natural pigments, giving its red color to blood (hemoglobin) or the green color to plants (chlorophylls). The electronic absorption spectra of porphyrins exhibit a characteristic pattern with π-π* transitions grouped into two distinct regions, the "Soret or B band", located between 380 and 450 nm, corresponds to a transition between the ground state and the second excited state (S_0-S_2). This transition is allowed by the selection rules and shows very high molar extinction coefficients ($\varepsilon > 10^5$ $M^{-1}\cdot cm^{-1}$). A shoulder sometimes appears on the high-energy side of the B band, attributed to one vibrational mode of excitation B (1-0). The so-called "Q bands" correspond to the S_0-S_1 transitions and are located between 500 and 750 nm, with molar extinction coefficients on the order of $\varepsilon = 10^3$ - 10^4 $M^{-1}\cdot cm^{-1}$. Generally, there are two or four Q bands depending whether it is a free base porphyrin or a metalloporphyrin.[14] The **Por(M)-H[6]^2** series was designed with the aim of changing the extent of the conjugation and the interchromophoric distance in order to modulate the chiroptical response by varying the intensity of the EC couplet and to examine

the metal contribution. The UV-vis absorption and ECD spectra were thus recorded in dichloromethane at a concentration of about 10^{-5} M (Figures 3a,b). The absorption spectra all display similar features, with contributions from the helicenic part and contributions from the porphyrin units. For instance, in the case of the free porphyrin **Por(H2)-H[6]^2**, a set of strong and broad bands are found between 230 and 380 nm with ε values within the range of 35-56 × 10^3 M^{-1} cm^{-1} which mainly correspond to the helicene-based π-π* transitions (*vide infra*). At 431 nm, a highly intense Soret band is found with ε values as high around 250-280 × 10^3 M^{-1} cm^{-1}, accompanied by four Q bands of moderate to strong intensities (ε ~ 7.5-36.1 × 10^3 M^{-1} cm-1) between 525 and 656 nm. Note that some vibronic progression was also observed since a total of 5 bands were found (see Figure 3b and Table 1). Slightly different absorption wavelengths were found between each metallated porphyrins. For instance, the Ni(II) complex had less delocalized π bonds which decreased the average electron density of the molecule and increased the energy available for electron transitions. Consequently, a blue shift occurred in the Soret bands (427 nm). The Zn(II) porphyrin possessed more delocalized π bonds which in turn lowered the energy required for electron transitions, leading to a slight red shift in the Soret band (436 nm). Overall, the Pd(II) and free porphyrin systems were found to exhibit stronger absorption spectra while the Zn(II) and Ni(II) systems showed similar and less intense absorption features. Note however that the absorptive responses are so intense that such measurements are accompanied by a substantial uncertainty and should be considered with caution. It thus appears safer to consider the dissymmetry factors which are inherent to the chiral molecule properties (see the g_{abs} values below).

The ECD spectra display similar characteristics as the UV-visible, exhibiting the same intensity changes in the signal at the Soret band (Figure 3a). The metalloporphyrins derivatives typically show only one ECD-active Q band, while the protonated chromophores exhibit two, as listed in Table 1 for *P* enantiomers. It is fundamental to highlight how the intensity of the Exciton Couplet increased in the system 2 where there is only an ethynyl spacer between the porphyrin and the helicene core, as compared to system 1. For instance, for *P*-**Por(Zn)-H[6]^2** the $\Delta\varepsilon$ value for the positive band of the couplet at the Soret band is 460 M^{-1} cm^{-1} while comparatively for the positive signal of the helicenic part (330 nm) is only 51 M^{-1} cm^{-1}. This is also nicely seen in the g_{abs} spectra plotted in Figure 3c which show stronger values on the porphyrin centered bands than on the helicenic ones. It is also worth to note from Figure 3c that all derivatives display very similar g_{abs} values for the Soret band, highlighting the fact that the distance between the two porphyrin units matters, not the metal. However, it is also interesting to highlight that the ECD bands centred around 350 nm, mainly involving the helicenic transitions (the so-called B-type transition),[15] show a doubly structured band whose intensities differ from one metal to another in the order Ni>Pd>Zn>H2 for the lower energy one, strongly suggesting that there is some influence of either electron-vibronic coupling and involvement of the porphyrin units in these transitions (*vide infra*) with an electronic density of the metal having an impact on the rotatory strengths.

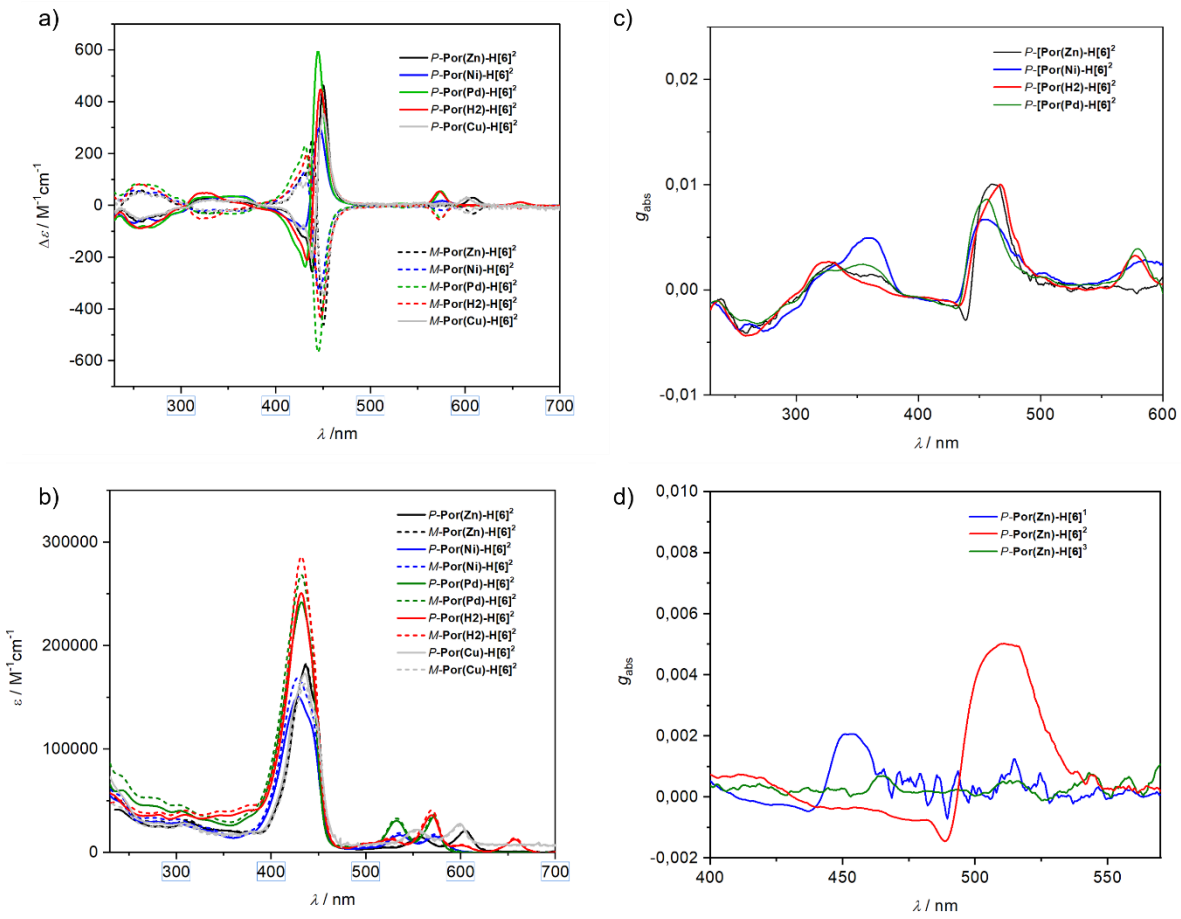

Figure 3. a) ECD and b) absorption spectra of the **Por(M)-H[6]^2** series, measured at room temperature in CH_2Cl_2 solutions. c) Comparison of g_{abs} spectra of the *P*-**Por(M)-H[6]^2** derivatives. d) Comparison of g_{abs} spectra of the *P*-**Por(Zn)-H[6]$^{1\text{-}3}$**.

Table 1. Molar absorption coefficients and $\Delta\varepsilon$ values for the Soret and Q bands of the *P*-**Por(M)-H[6]^2** derivatives in CH_2Cl_2 solutions at room temperature.

Metal	UV-vis Soret band λ (nm), ε (10^4 x M^{-1} cm^{-1})	ECD Soret band λ (nm), $\Delta\varepsilon$ (M^{-1} cm^{-1})	UV-vis Q bands λ (nm), ε (103 x M^{-1} cm^{-1})	ECD Q bands λ (nm), $\Delta\varepsilon$ (M^{-1} cm^{-1})
P-**Por(H2)-H[6]^2**	431 nm, 25.0	434, -201; 448, +450	502, 9.2; 526, 12.7; 570, 36.1; 601, 7.5; 656, 12.4	570, +58
P-**Por(Zn)-H[6]^2**	436 nm, 18.1	437, -249; 450, +460	556, 15.2; 604, 20.7	607, +32
P-**Por(Ni)-H[6]^2**	427 nm, 15.0	427, -84; 446, +300	535, 16.7; 572, 15.7	538, +12; 575, +20
P-**Por(Pd)-H[6]^2**	431 nm, 24.2	430, -233; 444, +602	495, 7.2; 532, 30.7; 573, 33.7	530, +12; 575, +61

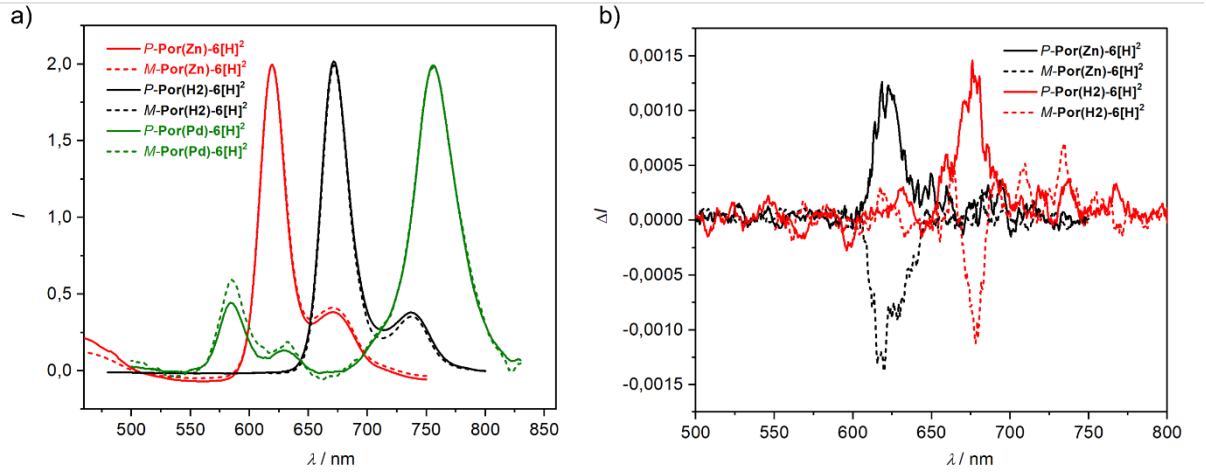

Figure 4. a) Emission and b) CPL spectra of the **Por(M)-H[6]²** series, measured at room temperature in CH_2Cl_2 solutions (see SI for further information).

Non-polarized and circularly polarized emission

The total luminescence of this family of compounds was investigated by measuring the emission of 10^{-6} M solutions in CH_2Cl_2, at room temperature (rt), with an excitation at 440 nm. The spectra are reported on Figure 4a. Unpolarized luminescence spectra of the **Por(M)-H[6]²** series were measured at room temperature in CH_2Cl_2 solutions for all the derivatives except for the Pd porphyrin for which the phosphorescence was investigated under inert atmosphere. As expected, the Ni derivative showed no emission properties, while the Zn and the free base porphyrins compounds displayed quite similar emission spectra, and in good agreement with literature: two emission bands at 620 and 670 nm for **Por(Zn)-H[6]²**, and at 670 and 738 nm for the free base **Por(H2)-H[6]²**, i.e. with a 50 nm red shift (see black and red line in Figure 4a). Pleasingly, these latter compounds were also found to be CPL-active (Figure 4b). Overall, the free base and the zinc complex display emission with rather good quantum yields around 30%, substantial g_{lum} values around 10^{-3} and good CPL brightness (Table 2). A different consideration should be made for the Pd and Cu derivatives. For the palladium porphyrin, the measurements were performed under inert atmosphere, in order to avoid oxygen quenching, and a predominant peak appeared at 750 nm, as depicted in Figure 4a. Some residual fluorescence signals were observed at 585 and 632 nm. However, no CPL could be detected with our instrument. Note that an interesting optically active cofacial ABCD-Pt(II)-porphyrin dimer was recently reported to display bright circularly polarized phosphorescence with $|g_{phos}|$ values of 1.0×10^{-3} and a quantum efficiency Φ of 0.07.[9i]

Table 2. Emission properties of *P*-**Por(M)-H[6]²** (M=H2, Zn) in CH_2Cl_2 and *P*-**Por(Zn)-H[6]³**. a) Relative quantum yield (TPP in dichloromethane as reference, see ESI); b) dissymmetry factor, g_{lum}, of each compound; c) CPL brightness.[16] Excitation at 440 nm for *P*-**Por(M)-H[6]²** (M=H2, Zn) and 410 nm for *P*-**Por(Zn)-H[6]³**.

Compound	PLQY[a]	g_{lum} (λ)[b]	ε_{440nm}	B_{CPL}[c]
P-**Por(Zn)-H[6]²**	0.28	1.1×10^{-3} (620 nm)	172×10^3	26
P-**Por(H2)-H[6]²**	0.32	1.3×10^{-3} (680 nm)	215×10^3	45
P-**Por(Zn)-H[6]³**	0.08	$\pm 1\times10^{-3}$	200×10^3	0.8

Synthesis of helicene-bis-ethynyl-phenyl porphyrin system (Por(Zn)-H[6]³)

2,5-Bis-ethynyl-carbo[6]helicene precursor was reacted with the spacer 1-bromo-4-iodobenzene upon classical Sonogashira conditions to give the dibrominated species **BrH[6]** in a 68 % yield (Scheme 2). On the other hand, the 5,15-(dimesityl)porphyrin was brominated, metalated and borylated using classical conditions, thus giving the corresponding boronate ester **Por(Zn)Bester**[17] (see SI). The so-obtained compounds were then involved in the Suzuki cross-coupling reaction to get the desired molecule **Por(Zn)-H[6]³** in a 40 % yield.

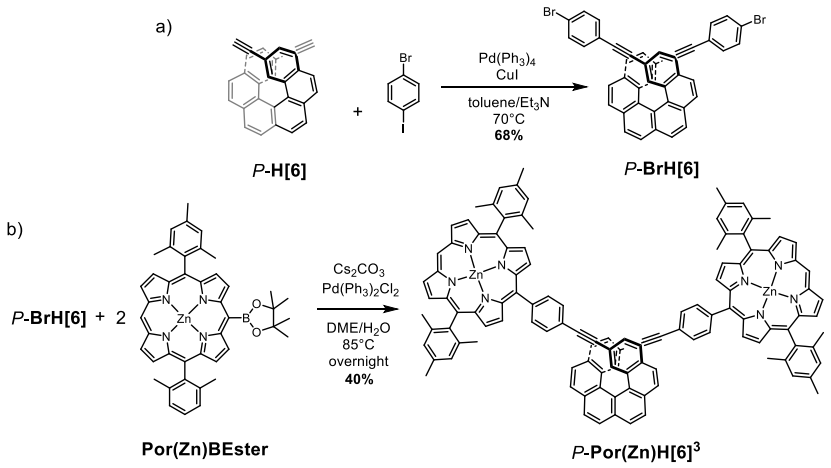

Scheme 2. a) Synthetic route for the helicene derivative **BrH[6]**; b) Suzuki coupling between the helicene **BrH[6]** and the porphyrin **Por(Zn)BEster** to give **Por(Zn)-H[6]³**.

As depicted on Figure S1.9, the ^{1}H NMR spectrum of **Por(Zn)-H[6]³** displays the typical signals for the helicene moiety and the two doublets of the phenyl protons of the spacer at 8.26 and 7.78 ppm. The porphyrin core show the same set of peaks as the previous compound **Por(Zn)-H[6]²**, with the proton of the free *meso* position resonating at 10.21 ppm and the β-pirrolic ones represented by the four doublets between 8.88 and 9.38 ppm. Since the porphyrin substitution has been modified, we observed a signal at 7.34 ppm corresponding to the aromatic protons of the mesityl unit, as well as two singlets at 1.88 and 2.69 ppm for the -CH_3 in ortho- and para- position of the mesityl unit, respectively.

UV-vis and ECD spectra of Por(Zn)-H[6]^3

The absorption spectrum of **Por(Zn)-H[6]^3** is depicted on Figure 5b. In the high-energy region, three absorption bands are observed at 300 nm (ε = 31260 M^{-1} cm^{-1}), 360 nm (ε = 16780 M^{-1} cm^{-1}), and 387 nm (ε = 20000 M^{-1} cm^{-1}), which can be assigned to π-π* transitions of the helicene unit; the Soret band appears at 414 nm (ε = 210755 M^{-1} cm^{-1}) and moving towards the low-energy region of the spectrum one signal for the Q bands of Zn porphyrins is observed at 541 nm (ε = 12860 M^{-1} cm^{-1}). Overall, it shows very similar features as for **Por(Zn)-H[6]^1**,[6] whose bridges differ only by an additional ethynyl spacer. Due to the variation in this conjugation extent, the signals undergo a blue shift of about 30 nm, and the molar extinction coefficients are lower. It is also worth to note that the porphyrins bear a phenyl in their *meso* position and it is known that small shifts may occur in the absorption maxima upon substitution in the para-positions of tetraphenylporphyrins.[18] Regarding the ECD (Figure 5a), the helicenic part is characterized by the typical negative ($\Delta\varepsilon$ = -73 M^{-1} cm^{-1} at 300 nm) and positive signals ($\Delta\varepsilon$ = + 12 and +75 at 267 and 369 nm, respectively) for the *P* enantiomer (opposite sign values are depicted for *M*-**Por(Zn)-H[6]^3**), as well as the bisignature of the exciton coupling for the Soret band (Δε = -38 at 407 nm and +112 at 420 nm). The overall ECD bands intensities are however more than twice lower compared to *M*-**Por(Zn)-H[6]^1**, revealing the beneficial implication of the triple bonds in the π-conjugated pathway and in the resultant optical activity.

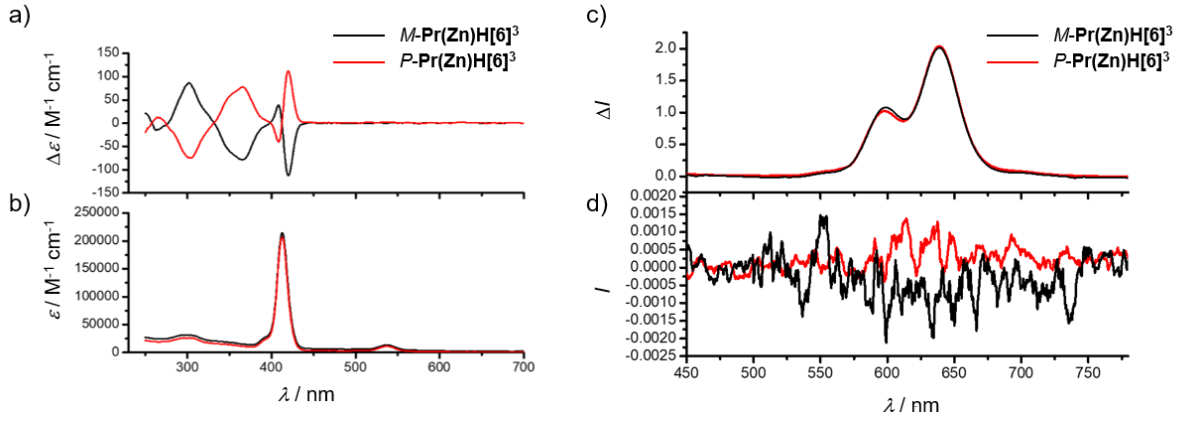

Figure 5. a) ECD and b) UV-vis spectra of **Por(Zn)-H[6]^3** in CH_2Cl_2 solutions at 298 K. c) Total luminescence and d) CPL spectra of **Por(Zn)-H[6]^3** in CH_2Cl_2 solution at 298 K.

The total luminescence spectrum showed two bands, a lower intensity band at 600 nm and a major one at 638 nm, which opposite intensity as for the previously described **Por(Zn)-H[6]^1** compound. In addition, **Por(Zn)-H[6]^3** was found CPL active, with a g_{lum} value of ± 1×10^{-3} but with a noisy signal (Figure 5d). The photoluminescence quantum yield of 0.08 was obtained in dichloromethane, using again TPP as reference. This value was found smaller compared to **Por(Zn)-H[6]^1**, highlighting again the importance of the triple bond present in the spacer to obtain strong emission through a stronger π-conjugation pathway. Note also that the brightness is much lower in **Por(Zn)-H[6]^3** than in the **Por(M)-H[6]^1** series (see Table 2).

Theoretical analysis and influence of Exciton Coupling in the Por(M)-H[6]^2 series

Full computational details can be found in Section S2 in the SI. In a nutshell, time-dependent density functional theory (TD-DFT) linear response theory was used to calculate absorption and ECD spectra with the ωB97X-D[19] range-separated hybrid functional and a split-valence polarized basis set SV(P). The ωB97X[32] functional was used to optimize the excited state geometries and to calculate the excited state harmonic frequencies and emission spectra because of unphysical geometries caused by the dispersion corrections in ωB97X-D. Regarding general strategies for calculating natural optical activity parameters, in particular with TD-DFT, see, for example, References 20 and 21.

The calculated vs. experimental absorption and electronic circular dichroism (ECD) spectra of the *M* isomers of compounds **Por(H$_2$)-H[6]^2**, **Por(Ni)-H[6]^2**, **Por(Zn)-H[6]^2**, and **Por(Pd)-H[6]^2** are shown in Figure 6. The excited-state optimizations and exciton-coupling calculations used the mesityl→Cl replacement model systems mentioned earlier (**Por(H$_2$)Cl-H[6]^2**, **Por(Ni)Cl-H[6]^2**, etc.), similar to a previous study of a related helicene-porphyrin system.[6] Section S2 in the SI shows extensive test calculations demonstrating that these substitutions do not affect the calculated absorption and ECD in the visible and near-UV spectral ranges because the mesityl groups absorb at shorter wavelengths. Consequently, except where necessary, the following discussion does not specifically distinguish between the full and the Cl-substituted systems. However, the compound **Por(Zn)-H[6]^3** was investigated without the substitution. The calculated UV-Vis and ECD spectra for the *M*-isomer of the compound is shown in SI Figure S2.8. A global energy shift of –0.25 eV was applied to all excitation energies prior to their conversion to wavelengths, to better align the calculated and experimental spectra. Energy shifts like this are typically necessary in calculations of helicene systems when range-separated hybrid functionals are employed.[6,22] We note in passing that range-separated hybrid functionals are recommended for porphyrin EC systems to avoid spurious charge-transfer transitions.[6,23] The energy-shifted calculated absorption and ECD spectra match the most intense experimental peaks both in terms of the absolute intensity as well as relative peak positions.

As experimentally observed, the absorption spectra of the systems are characterized by three groups of bands, namely helicene-centered, porphyrin-based Soret (B), and porphyrin Q bands. The calculated spectra are in satisfactory agreement with the experiments, with some deficiencies in the Q-band regions that were previously noted also for tetraphenyl-porphyrin (TPP): a selection of different functionals, including non-hybrid, global hybrid, and range-separated hybrids, were not able to reproduce the experimentally observed splitting between the Q band peaks,[22] which is also seen in the present calculations. Accordingly, in the low-energy region (> 550 nm), ωB97X-D predicts multiple transitions, as evident in the 'stick spectra' shown in Figures S2.13-S2.17 in the SI, but only one peak with the chosen broadening. The calculations describe the spectral region of the Soret band well, with four excitations underlying the high-intensity band. The high-energy part of the spectrum (< 300 nm) is also satisfactorily reproduced. For **Por(Zn)-H[6]^3**, the four dominant excitations in the Soret bands are well accounted for. However, the Q-bands are conspicuous by their absence both in the experimental and in the calculated spectrum (SI Figure S2.17).

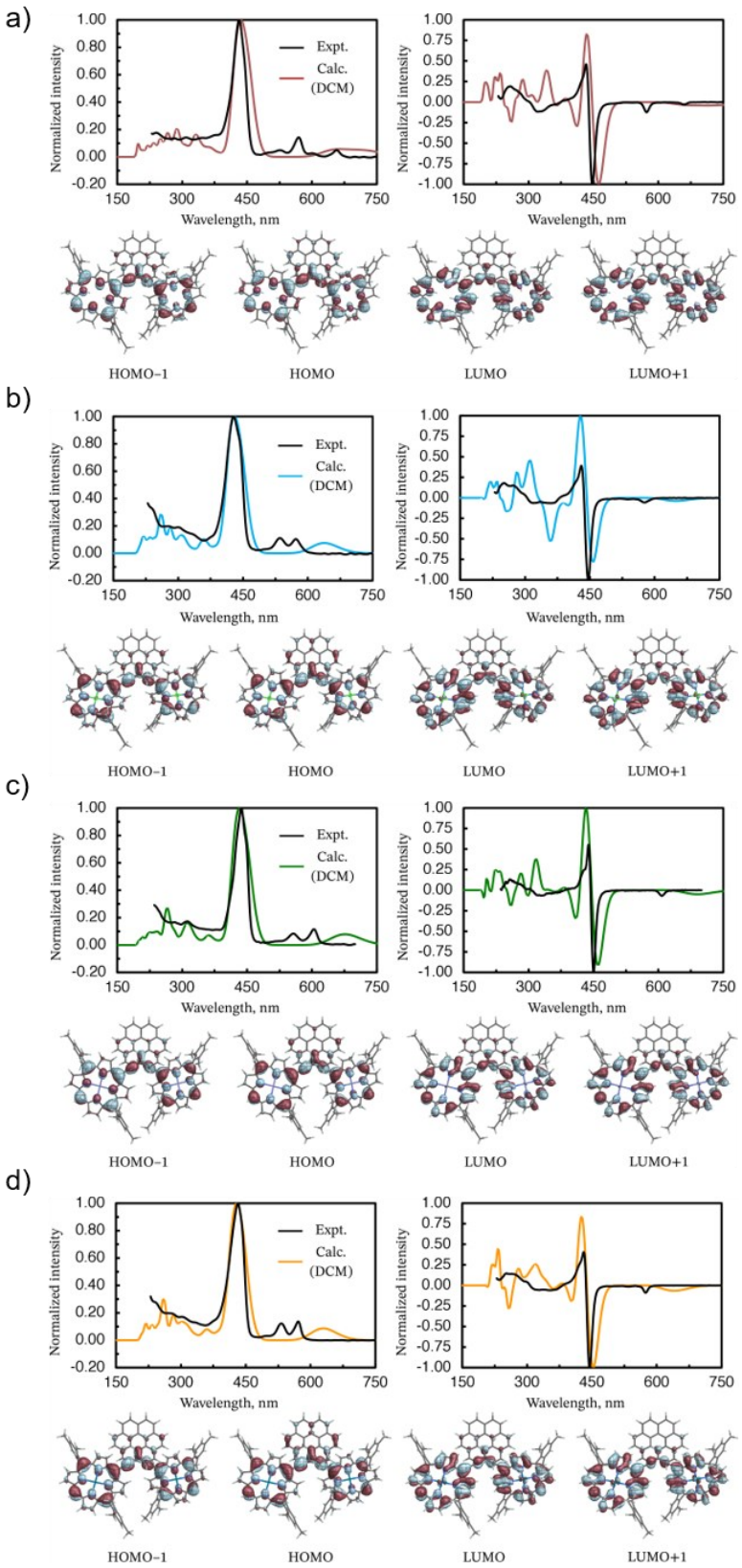

Figure 6. Experimental and calculated absorption (top left) and ECD (top right, *M* isomer) spectra and bottom: frontier molecular orbitals of the S_0 structure of a) **Por(H_2)-H[6]^2**, b) **Por(Ni)-H[6]^2**, c) of **Por(Zn)-H[6]^2**, and d) **Por(Pd)-H[6]^2** in CH_2Cl_2.

The calculated ECD spectrum of *M*-**Por(H$_2$)-H[6]^2** is dominated by what appears to be an exciton couplet (EC) peak structure around 450 nm associated with the porphyrin Soret bands. Additional calculations were performed on model systems in which the helicene moiety and the alkynyl bridges were removed, to understand how the presence of the helicene influences this dominant spectral feature. To summarize a large set of calculated data, as detailed in Section S2.4 in the SI, although the porphyrin rings in their relative orientations in **Por(H$_2$)-H[6]^2** are responsible for some of the ECD intensity observed in 450 nm region, the intensity of the exciton couplet is considerably stronger when the helicene is present. Therefore, the ECD intensity in this spectral region cannot be explained simply by EC of the porphyrin Soret band transitions, as we hypothesized initially. This finding lets us conclude that there must be substantial interactions between the helicene core and the porphyrin as far as the electronic transitions are concerned. On a related note, the negative sign of the ECD Q-band is correctly reproduced by the calculations on the full systems. The Q-band ECD intensity becomes significantly reduced when one of the porphyrin rings is removed, and the ECD becomes negligible on the scale of the plots when the helicene moiety and alkenyl bonds are removed. The influence from the helicene on the porphyrin Q-band EC ECD therefore likewise appears to be rather strong.

The calculated ECD spectra of the metalloporphyrin systems (nickel, zinc, and palladium) display qualitatively the same features as the **Por(H$_2$)-H[6]^2** spectrum. Some differences between the calculated and experimental spectra are observed in the low-energy region, where only one negative band (around 600 nm) is observed instead of two for the *M* enantiomer. The position of the calculated peak is slightly shifted towards higher wavelengths, but the intensity and the sign correctly match the experiments. In the Soret band region, the calculated and experimental bands have similar intensities for **Por(Zn)-H[6]^2** and **Por(Pd)-H[6]^2**, but they appear somewhat overestimated for **Por(Ni)-H[6]^2**.

Notably, the calculated ECD spectrum for **Por(Zn)-H[6]^3** which is shown in Figure S2.17 with absolute intensities, does not indicate a dramatic change in the intensity of the ECD Soret bands as a function of the (relatively minor) differences in the distance between the two porphyrin moieties when compared to the Series 2 analog. A factor that may be of relevance here is the interplay between the Davydov splitting and the rotatory strengths of the coupled transitions at the intermediate porphyrin distances encountered in the present systems. Namely, the resulting broadened intensity of the EC couplets is sensitive to these parameters. Certainly, however, given the aforementioned important and very strong helicene contributions to these bands, a simple long-range EC-ECD intensity decrease with increasing porphyrin distance is perhaps not to be expected. Instead, the computations indicate that the situation is more complex.

Further analysis of the excitations reveals that the orbitals in the transitions of the Soret band region are mainly centered on the porphyrin systems. However, contributions from the helicene rings are clearly visible, which bolsters the notion that the helicene directly takes a strong influence on the porphyrin EC couplets. The helicene contributions are evident in Figure 6, which shows the HOMO–1, HOMO, LUMO, and LUMO+1 for **Por(H$_2$)-H[6]^2**, **Por(Ni)-H[6]^2**,

Por(Zn)-H[6]², and **Por(Pd)-H[6]²**. The excitations in the high-energy region of the spectra mix contributions from the porphyrin rings and the helicenes more strongly.

Experimental circularly polarized luminescence (CPL) data are available for **Por(H₂)-H[6]²**, **Por(Zn)-H[6]²**, and **Por(Pd)-H[6]²**. The S_1 equilibrium structures of the Cl-substituted molecules (*M* isomers) were optimized using TDDFT. The fluorescence and CPL spectra, corresponding to the S_1 to S_0 transition, were calculated for the molecules and are shown in SI Figure S2.13-2.15. The two bands (one between 600-700 nm and another between 700-800 nm) in the emission spectra of **Por(H₂)-H[6]²** and **Por(Zn)-H[6]²** are well reproduced by the calculations. In the case of **Por(Pd)-H[6]²**, the calculation only produces the intense lowest-energy band located between 700-800 nm. It is at present unclear what might be the origin of the CPL observed experimentally at shorter wavelenghths. We note in passing that the calculated CPL spectra of the compounds **Por(H₂)-H[6]²**, **Por(Zn)-H[6]²** and **Por(Zn)-H[6]³** have the same sign (negative for the M isomer) as the intense ECD band at lower energies.

CISS effect measurements: mc-AFM

Since magnetic conductive AFM (mc-AFM) measurements involve the deposition of chiral molecules on a gold-coated nickel surface (Au/Ni), the arrangement of these molecules on the surface significantly impacts the efficiency of spin filtering. However, achieving precise molecular orientation is challenging. To address this, two main approaches were pursued: generating self-assembled monolayers (SAMs), using chiral molecules with anchoring groups such as –SH or –OH,[24] and harnessing flat, π-conjugated molecules that can autonomously organize into chiral, columnar arrangements.[25] In the first approach, the selectivity of spin is measured along the primary axis of the molecule, which stands perpendicular to the plane of the substrate. In contrast, the second approach involves polymers arranged on the Au/Ni surface, and the measurement of the CISS effect is taken perpendicular to the molecule's primary axis. However, both methodologies exhibit certain limitations. Approach (a) necessitates intricate modifications either before or after synthesizing the chiral molecule, while approach (b) requires meticulous design and extensive assessment of the supramolecular polymer's properties. Considering these challenges, finding new spin filters that are suitable compromises between easy processability and high performance is crucial to enable the practical application of the CISS effect in devices.

Thanks to the compromise between a high g_{abs} value and the significant Δε for the exciton couplet at the Soret band, **Por(Zn)-H[6]²** (see comparison on Figure 3d) was selected as suitable candidate for the CISS effect measurements through mc-AFM. The substrates for the mc-AFM studies were prepared using the e-beam evaporation deposition technique on Si (100) wafer. A 100 nm layer of Ni layer and a 7 nm layer of Au layer was deposited on a Si wafer: the gold layer has the function to protect Ni from oxidizing. The deposited multilayer surfaces were cleaned by immersing them first in acetone and then in ethanol for 10 minutes. The role of the Ni/Au surfaces is to allow spin polarization of electrons injected from the surface into the chiral molecules induced by a magnetic field.

The chiral molecules were deposited on the Ni/Au surfaces by spin coating a 1 mM solution in dichloromethane with at 3000 rpm for 40 sec. The mc-AFM images showed an amorphous nanoparticles-like assembly of the molecules onto the substrate (Figure 7). The calculation of the roughness of the surfaces was implemented using an higher resolution AFM.

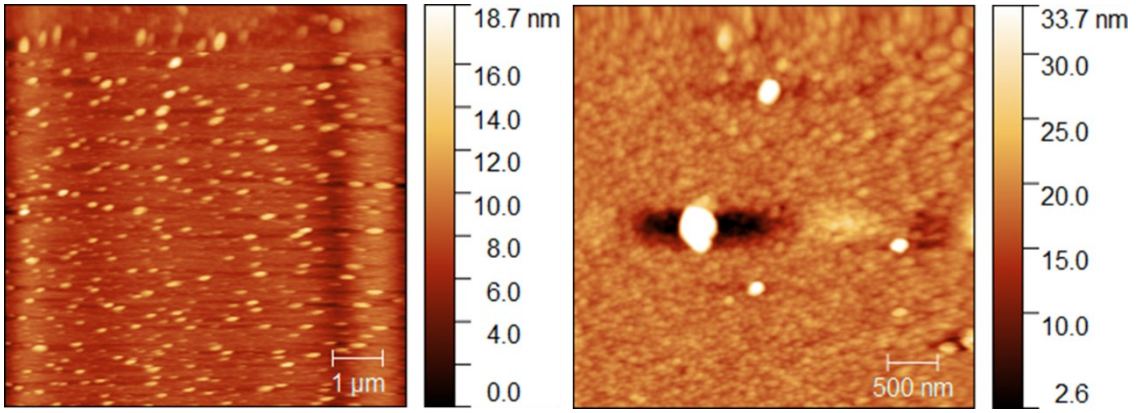

Figure 7. AFM images of the Ni/Au coated with *P*-**Por(Zn)-H[6]²**.

The gold-coated nickel surface (Au/Ni), with the chiral molecules, was magnetized perpendicularly to the surface, with the north pole pointing either up (toward the surface) or down. Depending on the direction of the external magnetic field (0.50 T), the spin of the ejected electrons from the nickel substrate to the deposited chiral molecular layer varies. The current displayed for both *M*- and *P*-**Por(Zn)-H[6]²** strong dependent on the direction of the magnetization of the substrate (Figure 8). Specifically, the *M*-enantiomer exhibits higher currents when the substrate is magnetized with the magnetic field up. In contrast, in the case of *P*-**Por(Zn)-H[6]²** the current is lower with the same magnetization but higher for magnetization down. These results are perfectly in line with former studies.[8]

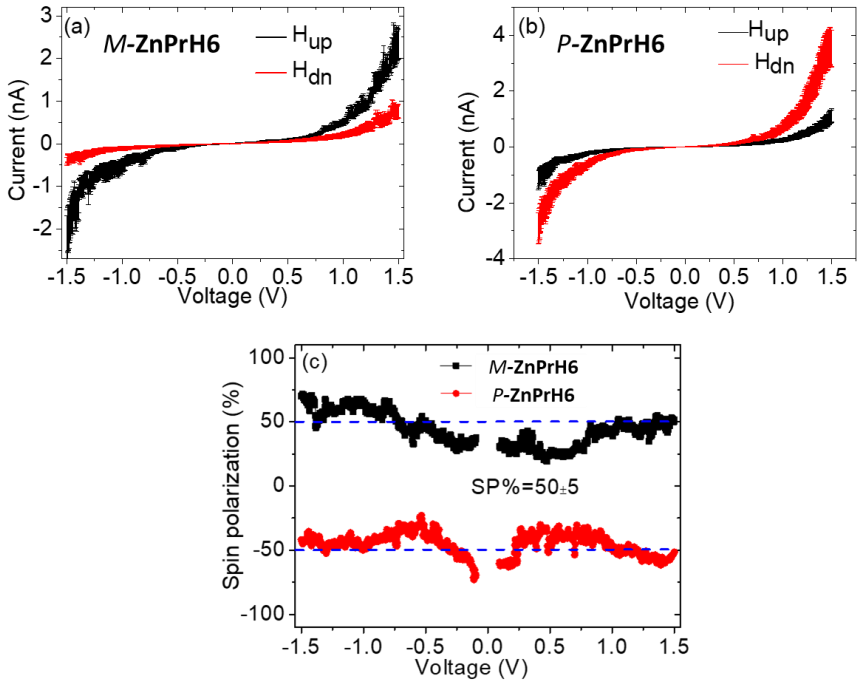

Figure 8. Current versus voltage (I-V) plots recorded for spin-coated (a) *P*-, and (b) *M* **Por(Zn)-H[6]²** on Ni-Au substrates. In both cases, the Ni substrates were magnetized with the north pole pointing in the up (the black line) and down (the red line) orientations; c) Spin Polarization plot for both compounds.

Magnetic field-dependent current-voltage (I-V) characteristics of the prepared samples were determined using a multimodal scanning magnetic probe microscopy (SPM) system equipped with a Beetle Ambient AFM and an electromagnet with an R9 electronic controller (RHK Technology). Voltage spectroscopy for the I-V measurements was performed by applying voltage ramps with a non-magnetic Pt tip (DPE-XSC11, µmasch with spring constant 3-5 Nm^{-1}) in contact mode. At least 50 I-V curves were scanned for each sample.

The spin selective electron transport was quantified (SP, spin polarization) as the relative ratio of currents with the two different configurations of the magnet (UP and DOWN),

$$SP = \frac{(I_{UP} - I_{DOWN})}{(I_{UP} \mp I_{DOWN})} \times 100 = 50 \pm 5\,\%$$

The SP value is about constant for the range of ±0.1 to ±1.5 V. Overall, the value is quite high considering that there are no anchoring groups or supramolecular polymerization or organization.

Conclusions

The chemical design of helicenes with porphyrin substituents allowed us to fine-tune this platform by changing the linker between the helicene and the porphyrin to achieve higher g_{abs} and g_{lum} values. A noteworthy enhancement was achieved with the family of molecules **Por(Zn)-H[6]²** where the 2,5-bis-ethynyl carbo[6]helicene is linked to the porphyrins avoiding

the spacer, so that the interchromophoric distance is reduced. In the ECD spectrum, the EC bisignature at the Soret band appeared to be the prominent signal compared to the helicene bands, and the g_{abs}/g_{lum} values were remarkably improved. Therefore, the investigation of the properties was extended to the influence of the metal and several derivatives were prepared. Within the same series '2', no significant changes were observed with the different metals, suggesting the exclusive role of the interchromophoric distance on the chiroptical response of the Soret band and further emphasizing the nature of the EC chirality in addition to π-conjugation with the helicene extremities. Interestingly, when adding a phenyl spacer, such as in **Por(Zn)-H[6]^3**, smaller EC responses were observed, in agreement with a longer interchomophoric distance. Derivative **Por(Zn)-H[6]^2** was selected as a favorable candidate for CISS measurements through mc-AFM and spin polarization as high as 50% was obtained. Overall, these results nicely illustrate how molecular engineering using functionalization with strongly polarizable units in close proximity enables the fine-tuning of the chiroptical signatures. This strategy also allows the access to CPL active porphyrin derivatives which still remains quite rare and opens up new opportunities for the design of new suitable candidates for spintronics applications.

Computational details

All quantum chemical calculations employed Kohn–Sham density functional theory (KS DFT) and time-dependent DFT (TD-DFT) linear response methods. Geometry optimizations (*M* isomers of all molecules) and harmonic vibrational frequency calculations for the ground states were performed with the B3LYP[26] hybrid generalized gradient approximation (GGA) functional and the Gaussian-type basis set def2-SV(P).[27] For the excited states, ωB97X was used to optimize the lowest excited state geometries. A scalar relativistic effective core potential (ECP) matching the def2-SV(P) basis was employed for the palladium atom. All structures were characterized as minima on their potential energy surfaces. The calculations were performed using the Conductor-like Polarizable Continuum Model (C-PCM)[28] with parameters for dichloromethane. All calculations were performed with the Gaussian 16 program.[29] See Section S2 in the SI for additional comments regarding the geometry optimizations performed herein. Absorption and electronic circular dichroism (ECD) spectra were calculated with TD-DFT. The transitions were Gaussian-broadened with a wavelength-dependent σ according to Reference 30.

Acknowledgments

We acknowledge the Ministère de l'Education Nationale, de la Recherche et de la Technologie, the Centre National de la Recherche Scientifique (CNRS), Rennes Métropole and the French National Agency (ANR projects LumoMat-E, 18-EURE-0012 and CHIFTS, ANR-23-CE09-0022-03). The European Commission Research Executive Agency (Grant Agreement number: 859752 − HEL4CHIROLED − H2020-MSCA-ITN-2019) is thanked for financial support. J.A. thanks the National Science Foundation for financial support of the theoretical component of this research from grant CHE-2503332. We acknowledge the Center for Computational Research (CCR) at the University at Buffalo[31] for providing computational resources. Part of this work has been performed using the PRISM core facility (Biogenouest, Univ Rennes, Univ Angers, INRAE, CNRS, FRANCE). JC warmly thanks Dr. Ludovic Favereau for fruitful discussions and technical help.

References

[1] a) C.-F. Chen, Y. Shen, *Helicene Chemistry: From Synthesis to Applications*, Springer Berlin Heidelberg: Berlin, Heidelberg, **2017**; b) M. Gingras, *Chem. Soc. Rev.* **2013**, *42*, 1051–1095; c) K. Dhbaibi, L. Favereau, J. Crassous, *Chem. Rev.* **2019**, *119*, 8846–8953 ; d) J. Crassous, I. G. Stará, I. Starý, *Helicenes - Synthesis, Properties and Applications,* Wiley, **2022**.

[2] a) R. Bouvier, R. Durand, L. Favereau, M. Srebro-Hooper, V. Dorcet, T. Roisnel, N. Vanthuyne, Y. Vesga, J. Donnelly, F. Hernandez, J. Autschbach, Y. Trolez, J. Crassous, *Chem. Eur. J.* **2018**, *24*, 14484–14494; b) K. Dhbaibi, L. Favereau, M. Srebro-Hooper, M. Jean, N. Vanthuyne, F. Zinna, B. Jamoussi, L. Di Bari, J. Autschbach, J. Crassous, *Chem. Sci.* **2018**, *9*, 735–742; c) K. Dhbaibi, L. Favereau, M. Srebro-Hooper, C. Quinton, N. Vanthuyne, L. Arrico, T. Roisnel, B. Jamoussi, C. Poriel, C. Cabanetos, J. Autschbach, J. Crassous, *Chem. Sci.* **2020**, *11*, 567–576; d) K. Dhbaibi, C. Shen, M. Jean, N. Vanthuyne, T. Roisnel, M. Górecki, B. Jamoussi, L. Favereau, J. Crassous, *Front. Chem.* **2020**, *8*, 237; e) C. Shen, F. Gan, G. Zhang, Y. Ding, J. Wang, R. Wang, J. Crassous, H. Qiu, *Mater. Chem. Front.* **2020**, *4*, 837–844; f) K. Dhbaibi, L. Abella, S. Meunier-Della-Gatta, T. Roisnel, N. Vanthuyne, B. Jamoussi, G. Pieters, B. Racine, E. Quesnel, J. Autschbach, J. Crassous, L. Favereau, *Chem. Sci.* **2021**, *12*, 5522–5533.

[3] a) N. Harada, K. Nakanishi, N. Berova, in *Comprehensive Chiroptical Spectroscopy*, John Wiley & Sons, Inc., **2012**, p. 115; b) N. Berova, L. D. Bari, G. Pescitelli, *Chem. Soc. Rev.* **2007**, *36*, 914–931; c) X. Huang, K. Nakanishi, N. Berova, *Chirality* **2000**, *12*, 237–255.

[4] G. Pescitelli, S. Gabriel, Y. Wang, J. Fleischhauer, R. W. Woody, N. Berova, *J. Am. Chem. Soc.* **2003**, *125*, 7613–7628.

[5] a) Dolphin, D. The Porphyrins; Academic Press: New York, **1979**. For a review on optically active porphyrins, see b) H. Lu, N. Kobayashi, *Chem. Rev.* **2016**, *116*, 6184-6261. For a seminal review on the spectra of porphyrins, see: c) M. Gouterman, *J. Mol. Spec.* **1961**, *6*, 138-163.

[6] K. Dhbaibi, P. Matozzo, L. Abella, M. Jean, N. Vanthuyne, J. Autschbach, L. Favereau, J. Crassous, *Chem. Comm.* **2021**, *57*, 10743–10746.

[7] B. Bloom, Y. Paltiel, R. Naaman, D. Waldeck, Chiral Induced Spin Selectivity, *Chem. Rev.* **2024**, *124*, 1950–1991.

[8] A) G. Bullard, F. Tassinari, C.-H. Ko, A. K. Mondal, R. Wang, S. Mishra, R. Naaman, M. J. Therien, *J. Am. Chem. Soc.* **2019***, 141*, 14707–14711; b) C.-H. Ko, Q. Zhu, F. Tassinari, G. Bullard, P. Zhang, D. Beratan, R. Naaman and M. Therien, *PNAS* **2022***, 119*, e2116180119.

[9] a) V. Kiran, S. P. Mathew, S. R. Cohen, I. Hernández Delgado, J. Lacour, R. Naaman*, Adv. Mater.* **2016**, *28*, 1957–1962; b) M. Kettner, V. V. Maslyuk, D. Nürenberg, J. Seibel, R. Gutierrez, G. Cuniberti, K.-H. Ernst, H. Zacharias, *J. Phys. Chem. Lett.* **2018**, *9*, 2025–2030; c) R. Rodríguez, C. Naranjo, A. Kumar, P. Matozzo, T.-K. Das, Q. Zhu, N. Vanthuyne, R. Gómez, R. Naaman, L. Sánchez, J. Crassous, *J. Am. Chem. Soc.* **2022**, *144*, 7709–7719; d) R. Rodríguez, C. Naranjo, A. Kumar, K. Dhbaibi, P. Matozzo, F. Camerel, N. Vanthuyne, R. Gómez, R. Naaman, L. Sánchez, J. Crassous, *Chem. Eur. J.* **2023**, *29*, e202302254; e) Y. Liang, K. Banjac, K. Martin, N. Zigon, S. Lee, N. Vanthuyne, F. Andrés Garcés-Pineda, J. R. Galán-Mascarós, X. Hu, N. Avarvari, M. Lingenfelder, *Nature Comm.* **2022**, *13*, 3356; f) N. Giaconi, L. Poggini, M. Lupi, M. Briganti, A. Kumar, T. K. Das, A. L. Sorrentino, C. Viglianisi, S. Menichetti, R. Naaman, R. Sessoli, M. Mannini, *ACS Nano* **2023**, *17*, 15189–15198; g) M. R. Safari, F. Matthes, C. M. Schneider, K.-H. Ernst, D. E. Bürgler, *Small* **2024**, *20*, 2308233; h) H. Jiang, D. Čavlović, Q. Jiang, F. Ng, S. T. Bao, E. J. Telford, M. L. Steigerwald, X. Roy, C. Nuckolls, J. M. McNeill, *J. Am. Chem. Soc.* **2025**, *147*, 12982−12988.

[10] a) J. M. Fox, T. J. Katz, S. V. Elshocht, T. Verbiest, M. Kauranen, A. Persoons, T. Thongpanchang, T. Krauss and L. Brus, *J. Am. Chem. Soc.* **1999**, *121*, 3453–3459; b) B. K. Mandal, T. Sooksimuang, *J. Porphyrins Phthalocyanines,* **2002**, *6*, 66–72; c) F. Zhang, K. Radacki, H. Braunschweig, C. L. P. Ravat, A*ngew. Chem. Int. Ed.* **2021**, *60*, 23656–23660; d) K. Kato, K. Furukawa, T. Mori, A. Osuka, *Chem. Eur. J.* **2018***, 24*, 572–575; e) B. Szyszko, M. Przewoźnik, M. J. Białek, A. Białońska, P. J. Chmielewski, J. Cichos, L. Latos-Grażyński, *Angew. Chem. Int. Ed.* **2018***, 57*, 4030–4034; f) V. Silber, N. Gruber, M. Jean, N. Vanthuyne, R. Ruppert, *Chem. Commun.* **2022**, *58*, 6012–6015; g) V. Silber, M. Jean, N. Vanthuyne, N. Del Rio, P. Matozzo, J. Crassous, P. Ruppert, *Org. Biomol. Chem.* **2023**, *21*, 8924–8935; h) S. Belviso, G. Marsico, R. Franzini, C. Villani, S. Abbate,

G. Longhi, Dalton Trans. **2022**, *51*, 16453–16464; i) R. Inoue, M. Kobayashi, Y. Morisaki, *Chem. Commun.* **2025**, *61*, 957-960.
[11] E. Anger, M. Srebro, N. Vanthuyne, L. Toupet, S. Rigaut, C. Roussel, J. Autschbach, J. Crassous, R. Réau, *J. Am. Chem. Soc.* **2012**, *134*, 15628–15631
[12] a) F. Mohajer, M. M. Heravi, V. Zadsirjana, N. Poormohammad, *RSC Adv.* 2021, **11**, 6885–6925; b) A. Soheili, J. Albaneze-Walker, J. A. Murry, P. G. Dormer, D. L. Hughes, *Org. Lett.* **2003**, *5*, 4191–4194; c) M. Gazvoda, M. Virant, B. Pinter, J. Košmrlj, *Nat. Commun.* **2018**, *9*, 4814.
[13] J. Hoard, *Science* **1971**, *174*, 295–1302.
[14] M. Goutermann, G. H. Wagniere, *J. Mol. Spectroscopy* **1963**, *11*, 108–127.
[15] a) F. Furche, R. Ahlrichs, C. Wachsmann, E. Weber, A. Sobanski, F. Vögtle, Stefan Grimme, *J. Am. Chem. Soc.* **2000,** *122,* 1717–1724; b) J. Wade, F. Salerno, R. C. Kilbride, D. Kuk Kim, J. A. Schmidt, J. A. Smith, L. M. LeBlanc, E. H. Wolpert, A. A. Adeleke, E. R. Johnson, J. Nelson, T. Mori, K. E. Jelfs, S. Heutz, M. J. Fuchter, *Nat. Chem.* **2022**, *14*, 1383–1389.
[16] L. Arrico, L. Di Bari, F. Zinna, *Chem. Eur. J.* **2021**, *27*, 2920–2934
[17] L. Yu, K. Muthukumaran, I. V. Sazanovich, C. Kirmaier, E. Hindin, *Inorg. Chem.* **2003**, *42*, 6629–6647.
[18] D. W. Thomas, A. E. Martell, *J. Am. Chem. Soc.* **1956**, *78*, 1338–1343.
[19] J. -D. Chai, M. Head-Gordon, Long-Range Corrected Hybrid Density Functionals with Damped Atomatom Dispersion Corrections. *Phys. Chem. Chem. Phys.* **2008**, *10*, 6615.
[20] J. Autschbach, L. Nitsch–Velasquez, L.; Rudolph, M. *Top. Curr. Chem.* **2011**, *298*, 1–98.
[21] M. Srebro-Hooper, J. Autschbach, *Annu. Rev. Phys. Chem.* **2017**, *68*, 399–420.
[22] a) B. C. Baciu, P. J. Bronk, T. de Ara, R. Rodriguez, P. Morgante, N. Vanthuyne, C. Sabater, C. Untiedt, J. Autschbach, J. Crassous, A. Guijarro, *J. Mater. Chem. C* **2022**, *10*, 14306–14318; b) P. Sumsalee, P. Morgante, G. Pieters, J. Crassous, J. Autschbach, L. Favereau, L. *J. Mater. Chem. C* **2023**, *11*, 8514–8523.
[23] B. Moore II, J. Autschbach, *ChemistryOpen* **2012**, *1*, 184–194.
[24]S. Mishra, A. K. Mondal, E. Z. B. Smolinsky, R. Naaman, K. Maeda, T. Nishimura, T. Taniguchi, T. Yoshida, K. Takayama, E. Yashima, *Angew. Chem. Int. Ed.* **2020**, *59*, 14671–14676.
[25] a) C. Kulkarni, A. K. Mondal, T. K. Das, G. Grinbom, F. Tassinari, M. F. J. Mabesoone, E. W. Meijer, R. Naaman, *Adv. Mater.* **2020**, *32*, 1904965; b) A. K. Mondal, M. D. Preuss, M. L. Ślęczkowski, T. K. Das, G. Vantomme, E. W. Meijer, R. Naaman, *J. Am. Chem. Soc.* **2021**, **143**, pp. 7189–7195.
[26] a) A. D. Becke, *Phys. Rev. A* **1988**, *38*, 3098–3100; b) C. Lee, W. Yang, R. G. Parr, *Phys. Rev. B* **1988**, *37*, 785–789; c) A. D. Becke, *J. Chem. Phys.* **1993**, *98*, 5648–5652.
[27] F. Weigend, R. Ahlrichs, *Phys. Chem. Chem. Phys.* **2005**, *7*, 3295–3305.
[28] a) V. Barone, M. Cossi, *J. Phys. Chem. A* **1998**, *102*, 1995–2001; b) M. Cossi, N. Rega, G. Scalmani, V. Barone, *J. Comput. Chem.* **2003**, *24* (6), 669–681.
[29] M. J. Frisch, G. W. Trucks, H. B. Schlegel, G. E. Scuseria, M. A. Robb, J. R. Cheeseman, G. Scalmani, V. Barone, G. A. Petersson, H. Nakatsuji, X. Li, M. Caricato, A. V. Marenich, J. Bloino, B. G. Janesko, R. Gomperts, B. Mennucci, H. P. Hratchian, J. V. Ortiz, A. F. Izmaylov, J. L. Sonnenberg, D. Williams-Young, F. Ding, F. Lipparini, F. Egidi, J. Goings, B. Peng, A. Petrone, T. Henderson, D. Ranasinghe, V. G. Zakrzewski, J. Gao, N. Rega, G. Zheng, W. Liang, M. Hada, M. Ehara, K. Toyota, R. Fukuda, J. Hasegawa, M. Ishida, T. Nakajima, Y. Honda, O. Kitao, H. Nakai, T. Vreven, K. Throssell, J. A. Montgomery, Jr., J. E. Peralta, F. Ogliaro, M. J. Bearpark, J. J. Heyd, E. N. Brothers, K. N. Kudin, V. N. Staroverov, T. A. Keith, R. Kobayashi, J. Normand, K. Raghavachari, A. P. Rendell, J. C. Burant, S. S. Iyengar, J. Tomasi, M. Cossi, J. M. Millam, M. Klene, C. Adamo, R. Cammi, J. W. Ochterski, R. L. Martin, K. Morokuma, O. Farkas, J. B. Foresman, D. J. Fox. Gaussian 16 Revision A.03.
[30]A. Brown, C. M. Kemp, S. F. Mason, *J. Chem. Soc. A* **1971**, 751–755.
[31] Center for Computational Research, University at Buffalo. URL http://hdl.handle.net/10477/79221. Accessed 11/2023.
[32] J. -D. Chai, M. Head-Gordon, *J. Chem. Phys.* **2008**, 128,084106.